

A Hydrogen-Initiated Chemical Epitaxial Growth Strategy for In-Plane Heterostructured Photocatalyst

Jinqiang Zhang,[†] Yunguo Li,[‡] Xiaoli Zhao,[†] Huayang Zhang,[§] Liang Wang,[#] Haijun Chen,^{||} Shuaijun Wang,[†] Xinyuan Xu,[†] Lei Shi,[†] Lai-Chang Zhang,[†] Jean-Pierre Veder,[⊥] Shiyong Zhao,[⊖] Gareth Nealon,[⊥] Mingbo Wu,[⊥] Shaobin Wang^{§*}, and Hongqi Sun^{†*}

[†]School of Engineering, Edith Cowan University, 270 Joondalup Drive, Joondalup, WA 6027, Australia

[‡]Department of Earth Sciences, University College London, Gower Street, London WC1E 6BT, UK

[§]School of Chemical Engineering, The University of Adelaide, Adelaide, SA 5005, Australia

[#]State Key Laboratory of Mater-Oriental Chemical Engineering, College of Chemistry and Chemical Engineering, Nanjing Tech University, Nanjing 210009, China

^{||} Jiangsu Key Laboratory of Process Enhancement and New Energy Equipment Technology, Jiangsu Engineering Laboratory of Energy Conservation and Environmental Protection Technologies and Equipment in Process Industry, School of Mechanical and Power Engineering, Nanjing Tech University, Nanjing 211816, China

[⊥]John de Laeter Centre, Curtin University, Perth, Western Australia 6102, Australia

[⊖]Fuels and Energy Technology Institute & Western Australia School of Mines: Minerals, Energy and Chemical Engineering, Curtin University, Perth, Western Australia 6102, Australia

[⊥]Centre for Microscopy, Characterisation and Analysis, The University of Western Australia, Crawley, WA 6009, Australia

[⊥]State Key Laboratory of Heavy Oil Processing, Institute of New Energy, College of Chemical Engineering, China University of Petroleum (East China), Qingdao, 266580, China

1
2
3 *Corresponding Authors: h.sun@ecu.edu.au (H Sun); shaobin.wang@adelaide.edu.au (S
4
5 Wang)

6
7
8
9
10 **ABSTRACT:** Integrating carbon nitride with graphene into a lateral heterojunction would
11
12 avoid the energy loss within the interlaminar space region on conventional composites. Up to
13
14 now, its synthesis process is limited to the bottom-up method which lacks the targeting and
15
16 homogeneity. Herein, we proposed a hydrogen-initiated chemical epitaxial growth strategy at
17
18 a relatively low temperature for the fabrication of graphene/carbon nitride in-plane
19
20 heterostructure. Theoretical and experimental analysis proved that methane *via in situ*
21
22 generation from the hydrogenated decomposition of carbon nitride triggered the graphene
23
24 growth along the active sites at the edges of confined spaces. With the enhanced electrical field
25
26 from the deposited graphene (0.5 %), the performances on selective photooxidation and
27
28 photocatalytic water splitting were promoted by 5.5 and 3.7 times, respectively. Meanwhile, a
29
30 7720 $\mu\text{mol/h/g}_{(\text{graphene})}$ hydrogen evolution rate was acquired without any co-catalysts. This
31
32 study provides an up-bottom strategy to synthesize in-plane catalyst for the utilization of solar
33
34 energy.
35
36
37
38
39

40 **KEYWORDS:** hydrogen-initiated chemical epitaxial growth, carbon nitride/graphene,
41
42 intralayer heterojunction, photocatalytic water splitting, photooxidation
43
44
45
46
47
48
49
50
51
52
53
54
55
56
57
58
59
60

1
2
3 Carbon nitride photocatalyst with the advantages of metal-free and visible light response has
4
5 been widely utilized into energy preparation,¹ pharmaceutical synthesis² and environmental
6
7 governance.³ However, intrinsic carbon nitride typically suffers from inefficient generation of
8
9 hot carriers, which results in low photocatalytic performance, as a result of the weak driving
10
11 force on photo induced excitons. Hybridization with graphene has been regarded as an effective
12
13 approach for the modification of carbon nitride without extra addition of metal elements.⁴ With
14
15 a high value of charge mobility ($\mu \approx 10,000 \text{ cm}^2/\text{Vs}$), graphene acts as an electron mediator and
16
17 diverts electrons once excited, realizing the faster separation and transfer of charge carriers.^{5,6}
18
19 Nevertheless, the interlaminar space region formed in the fabricated heterojunction provides
20
21 rooms for the relaxation of electron-hole pairs.⁷ Therefore, spaces on improving the
22
23 photocatalytic performances of graphene/carbon nitride heterojunctions still exist.

24
25
26 Inosculating carbon nitride and graphene within in-plane interfaces might hold the promise
27
28 to shorten the transportation path of photo induced charge carriers in comparison of passing
29
30 through the interlaminar space region in van der Waals heterojunctions.⁸⁻¹⁰ Thus this more
31
32 rational photocatalyst in theory has always been a pursuit in the field of materials science. Based
33
34 on this, Che *et al.* employed a bottom-up method to obtain (C_{ring})- C_3N_4 plane heterostructural
35
36 nanosheets.¹¹ Despite of enhanced performance on this in-plane heterostructure, the targeting
37
38 and homogeneity of formed graphene on carbon nitride substrate cannot be guaranteed. Current
39
40 reasonable strategies for the fabrication of uniform intralayer heterostructures are mainly
41
42 dependent on the chemical epitaxial growth (CEG) or physical vapour deposition (PVD)
43
44 strategies.^{8,10,12} However, it is rarely reported on the fabrication of graphene/organic
45
46 semiconductor intralayer heterojunctions. On one side, the requirement of tremendous
47
48 compatibility on the lattice constants and lattice symmetry from each component of intralayer
49
50 heterostructures pose difficulties on its construction and on the other side processing conditions
51
52 such as temperature for both sides' stabilization are extremely uncontrollable.^{9,10} More
53
54 seriously, these requirements can not always be achieved at the same time.
55
56
57
58
59
60

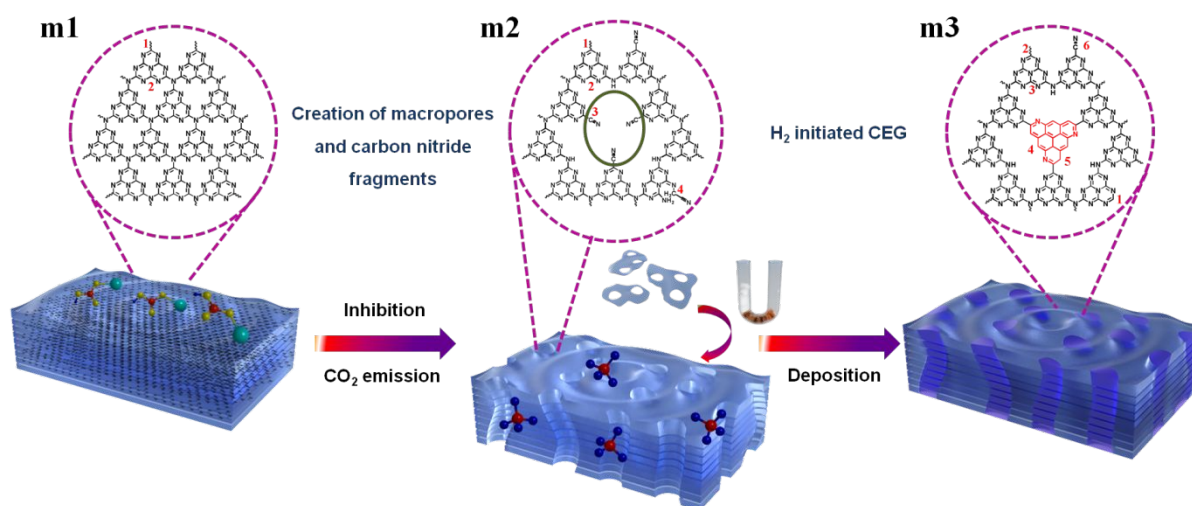
1
2
3 Herein, we proposed a hydrogen-initiated chemical epitaxial growth strategy at a relatively
4 low temperature for the fabrication of graphene/carbon nitride intralayer photocatalyst. Our
5 proof-of-concept demonstration is initially on the basis of the exceptionally similar molecular
6 configuration on carbon nitride and graphene. As demonstrated in Figure S1, both lattices of
7 this ‘wistedtwins’ have a hexagonal symmetry with similar space group, and the difference in
8 each lattice parameter is only 1.4 %, proving the feasibility of material construction. Moreover,
9 considering the pyrolysis temperature of carbon nitride (starting from 600 °C) is far below the
10 temperature for graphene formation (above 1000 °C using CVD method),^{13,14} confined spaces
11 and active sites, which are theoretical and experimental evidenced to be indispensable on
12 graphene deposition at relatively low temperature, were created on carbon nitride substrate.
13
14 After connecting the carbon rings of graphene with the tri-s-triazine units within carbon nitride,
15 the acquired in-plane heterojunction was found to exhibit enhanced electrical field and a more
16 favourable electronic structure for facilitating carriers’ separation and transfer. With the trace
17 amount of deposited graphene (0.5 %), the performances on selective photooxidation and
18 photocatalytic water splitting were promoted to be 5.5 and 3.7 times, respectively. In particular,
19 this in-plane heterostructure exhibited a 7720 $\mu\text{mol h}^{-1} \text{g}^{-1}_{(\text{graphene})}$ hydrogen evolution rate
20 without noble metal as co-catalyst.
21
22
23
24
25
26
27
28
29
30
31
32
33
34
35
36
37
38
39
40
41
42

43 RESULTS AND DISCUSSION

44
45
46 The fabrication process of graphene/carbon nitride intralayer heterojunction includes two
47 processes (Figure 1), *i.e.* the creation of confined spaces with active sites at edges on bulk
48 structure and the H₂ initiated CEG procedure for graphene formation. At first, a soft template
49 of sodium bicarbonate was added into a melamine solution followed by heating, another
50 molecule (Figure S2) was synthesized and subsequently heated with unreacted sodium
51 bicarbonate and melamine. During the polymerization process, apparent pore channels were
52 created on 10%-C₃N₄ and 14%-C₃N₄ (also named as porous carbon nitride) *via* the released
53
54
55
56
57
58
59
60

1
2
3 CO₂ from the pyrolysis of sodium bicarbonate,¹⁵ which could be confirmed from the
4 disappeared (100) peak from XRD profiles (Figure S3) and the appeared pores from electron
5 and atomic force microscopy images (Figure S4-6). Meanwhile, as the intercalating effect of
6 Na⁺ from sodium bicarbonate,¹⁶ a gradual decline can be observed in the (002) peak of porous
7 carbon nitride with increasing proportions of soft template (Figure S3), which is indicative of
8 breaking of van der Waals bonding within the layers of bulk carbon nitride.¹⁷ Since the
9 generated molecules in the precursor contain acylamino groups at edges (Figure S2), which
10 could act as a polymerization inhibitor in the polymerization process of carbon nitride.
11 Therefore, a large number of small and thin carbon nitride fragments with thickness less than 1
12 nm appeared (Figure S4c and 4g). These fragments can be gradually hydrogenated into methane
13 at 500 °C in H₂ atmosphere, which cannot otherwise be achieved in N₂ (Figure S7). It is known
14 that methane is the carbon gas source in the CEG process for graphene synthesis. Thus the
15 porous carbon nitride was thermally treated in hydrogen at 500 °C. After the hydrogenation
16 process, small carbon nitride fragments disappeared and the thickness of H₂-10%-C₃N₄ and H₂-
17 14%-C₃N₄ (also named as hydrogenated carbon nitride) exhibited an improved tendency
18 compared to that of porous carbon nitride (Figure S4d, S4h and S8). Same phenomenon can
19 also be observed on TEM and SEM images (Figure S9-10), especially on H₂-14%-C₃N₄ (Figure
20 S9d), a partial hydrogenated state that some pores were not completely patched was recorded.
21 Therefore, we reckon that the decomposition of the small fragments in hydrogen released
22 methane, which then *in situ* formed graphene along the edge of pores (confined spaces) to
23 produce a unique intralayer graphene/carbon nitride heterostructure. On this occasion, the
24 volumes of three samples, g-C₃N₄, 10%-C₃N₄, and H₂-10%-C₃N₄, at the same mass were
25 compared (Figure S10f), revealing that the column volume of 10%-C₃N₄ significantly increased
26 because of the exfoliation and porosity. However, the volume of H₂-10%-C₃N₄ decreased to
27 almost the same as that of g-C₃N₄, indicating the lose of porosity due to the graphene filling.
28 Same conclusion can also be reached from the BET results (Figure S11). By contrast, with less
29
30
31
32
33
34
35
36
37
38
39
40
41
42
43
44
45
46
47
48
49
50
51
52
53
54
55
56
57
58
59
60

1
2
3 pore maker of NaHCO_3 in the first step of Figure 1, no obvious damage can be observed on 2%-
4 C_3N_4 and 6%- C_3N_4 , which still remained the bulk structure (Figure S5-6). While after the
5
6 C_3N_4 and 6%- C_3N_4 , which still remained the bulk structure (Figure S5-6). While after the
7
8 calcination under H_2 atmosphere, the (002) peak intensity of both H_2 -2%- C_3N_4 and H_2 -6%-
9
10 C_3N_4 (Figure S8) experienced further decrease and their surface areas increased by two and
11
12 three times, respectively, as compared with that of g- C_3N_4 (Figure S11 and Table S1). This
13
14 confirms the further exfoliation, rather than the formation of graphene, occurred on 2%- C_3N_4
15
16 and 6%- C_3N_4 without confined spaces. Therefore, porous carbon nitride (10%- C_3N_4 and 14%-
17
18 C_3N_4) and hydrogenated carbon nitride (H_2 -10%- C_3N_4 and H_2 -14%- C_3N_4) will be emphatically
19
20 discussed in this work.
21
22



23
24
25
26
27
28
29
30
31
32
33
34
35
36
37
38
39
40
41 **Figure 1. Schematic illustration of the formation processes of intralayer heterojunctions.**
42
43 **m1, m2 and m3 are the proposed molecular structures of g- C_3N_4 , porous carbon nitride**
44
45 **and hydrogenated carbon nitride, respectively.**
46
47
48

49
50 The microscopic changes during this modified CEG process are initially supported by the
51
52 NMR spectra (Figure 2a): on pristine g- C_3N_4 , two main peaks at 165 and 155 ppm are evident,
53
54 corresponding to the carbon atoms at position 1 and the position 2 in m1, respectively (Figure
55
56 1). In addition to these two main peaks, there is an obvious peak centered at approximately 40
57
58 ppm on porous carbon nitride, which is attributed to the CH_2 group (position 4 in m2), indicating
59
60 the tri-s-triazine unit of the porous carbon nitride is destroyed. Besides, acylamino groups in

1
2
3 the precursor could convert into cyano groups because of the dehydration effect during the
4 polymerization (130 ppm in Figure 2a).¹⁸ As a result, this damage process forms one kind of
5 intralayer heterostructure as shown in m2. This structure is also reflected by the increased value
6 in Zeta potential of porous carbon nitride as the cyano groups have a strong electron-
7 withdrawing ability (Table S1). Whereas after the hydrogenation process, the signal of the CH₂
8 group on porous carbon nitride disappeared, with a peak emerging at 171 ppm, assigned to the
9 methine carbon at position 1, structure m3.¹⁹ This suggests that the damaged tri-s-triazine unit
10 is repaired. Noticeably, an peak at 137 ppm associated with sp² carbon also emerged, consistent
11 with the formation of graphene during the hydrogen treatment.²⁰ As a result, another intralayer
12 heteojunctions connected by the *in situ* generated graphene are produced. Apart from this, a
13 peak at 32.5 ppm was also found on H₂-10%-C₃N₄, which originates from the sp³ carbon
14 (position 5 in m3). XPS and FTIR studies were also performed to elucidate the changes of
15 chemical states and surface composition of the prepared samples. As observed from C1s spectra
16 (Figure S12), the peak at 285.4 eV assigned to amino groups on g-C₃N₄²¹ upshift to 286 eV on
17 14%-C₃N₄ after the damage process. Meanwhile the peak intensity gradually increases from
18 2.64 % on g-C₃N₄ to 6.18 % on 14%-C₃N₄, suggesting that the marginal amino groups of g-
19 C₃N₄ gradually changed to cyano groups with the increasing amount of soft template, since
20 cyano groups have the similar C1s binding energy to that of amino groups.¹⁸ This can also be
21 proven by the FTIR spectra (Figure S13), where the peak intensity of cyano groups at 2173
22 cm⁻¹ turns stronger and that of amino groups at 3090 cm⁻¹ becomes lower with more soft
23 template being added in the damage process.²² Besides, it was interesting to note that the ratio
24 between C=N and C=C bonds remained unchanged on all of the products after the damage
25 process (Figure S12b), suggesting that no obvious changes occurred on the tri-s-triazine unit of
26 the basal plane of carbon nitride. While on the hydrogenated samples, the ratio of C=C to C=N
27 bonds rose from 0.23 in g-C₃N₄ to 0.36 in H₂-10%-C₃N₄, verifying the growth of graphene
28
29
30
31
32
33
34
35
36
37
38
39
40
41
42
43
44
45
46
47
48
49
50
51
52
53
54
55
56
57
58
59
60

(Figure 2b and S14). Based on the NMR, XPS and FT-IR results, the possible molecular structures of the prepared samples are proposed in Figure 1.

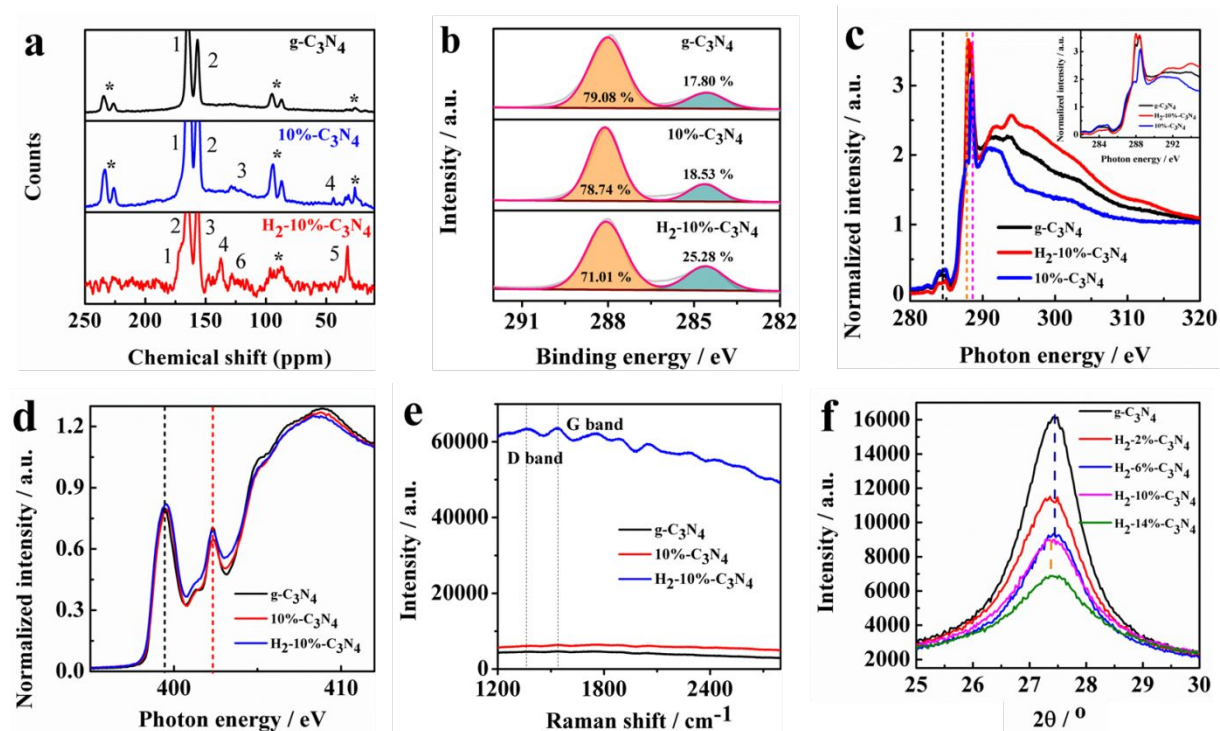


Figure 2. Microscopic evidences of the formation of graphene/carbon nitride intralayer heterojunction. (a) ^{13}C solid-state NMR spectra. (b) $\text{C}1\text{s}$ XPS spectra. (c-d) NEXAFS results. (e) Raman spectra and (f) Magnified XRD patterns of as-prepared samples.

The presence of graphene in the hydrogenated carbon nitride is confirmed by synchrotron-based near edge X-ray absorption fine structure (NEXAFS) spectroscopy measurements. All the samples show peaks at 284.5, 288 and 288.4 eV in C K-edge spectra (Figure 2c) which are the characteristic resonances of the defective carbon, $\pi^*_{\text{C}=\text{C}}$ and $\pi^*_{\text{C}=\text{N}-\text{C}}$, respectively.⁴ For the peak at 284.5 eV, the order of intensities from low to high is $\text{H}_2\text{-}10\%\text{-C}_3\text{N}_4$, $\text{g-C}_3\text{N}_4$ and $10\%\text{-C}_3\text{N}_4$, indicating that more carbon defects existed in the porous carbon nitride, and following hydrogenation, some of the defects were repaired. For the peak at 288 eV, small protuberances could be observed in $\text{g-C}_3\text{N}_4$ and $10\%\text{-C}_3\text{N}_4$ whereas $\text{H}_2\text{-}10\%\text{-C}_3\text{N}_4$ exhibited a single distinct peak, which demonstrates the successful deposition of the intraformational carbon ring in the basal plane of carbon nitride. In the N K-edge spectra (Figure 2d), two obvious peaks at 399.4

1
2
3 and 402.3 eV can be observed which are respectively the π^* resonances of C=N-C and C-N
4 bonding. The reduced peak intensity at 402.3 eV on H₂-10%-C₃N₄ also confirmed that the N-
5 3C bonding were substituted by the C=C bonding from graphene, which is consistent with the
6 C K-edge results. The same conclusion can also be drawn from Raman spectroscopy. As shown
7 in Figure 2e, distinct peaks of D (1370 cm⁻¹) and G (1540 cm⁻¹) bands can be seen on H₂-10%-
8 C₃N₄ which are not evident in the graphitic carbon nitride and 10%-C₃N₄ samples, indicating
9 the existence of graphitic carbon and defective carbon (mainly N doped carbon).²³ Besides, in
10 XRD profiles, although the intensity of the (002) peaks in hydrogenated carbon nitride exhibited
11 increased tendency compared with that of porous carbon nitride (Figure S8), the (100) peaks
12 also fail to re-emerge, confirming the absence of the CN polymer in the filled macropores of
13 the porous carbon nitride. More importantly, the (002) peaks of H₂-10%-C₃N₄ and H₂-14%-
14 C₃N₄ shift slightly from 27.4° in g-C₃N₄ to 27.3° (Figure 2f), indicating the existence of carbon
15 in the inplanar of carbon nitride.²⁴ These combined results clearly show the derivation of g-
16 C₃N₄ structure in the modified CEG processes, in which graphene grows along the edge plane
17 of porous carbon nitride from methane *via* hydrogenation of carbon nitride fragments.

18
19 Furthermore, different from the porous sample (Figure S15), uneven distributions of C and
20 N elements on H₂-10%-C₃N₄ are evident, and carbon-rich areas are easily discernable (Figure
21 3). Correspondingly, in EDX spectra some areas of H₂-10%-C₃N₄ obey the same C/N ratio as
22 that in the porous carbon nitride and some areas contain less N. The high-resolution TEM
23 images (Figure 3c and Figure S16) confirm an interlayer crystal lattice in hydrogenated carbon
24 nitride which locates within the position of macro-pore in porous carbon nitride. The
25
26
27
28
29
30
31
32
33
34
35
36
37
38
39
40
41
42
43
44
45
46
47
48
49
50
51
52
53
54
55
56
57
58
59
60

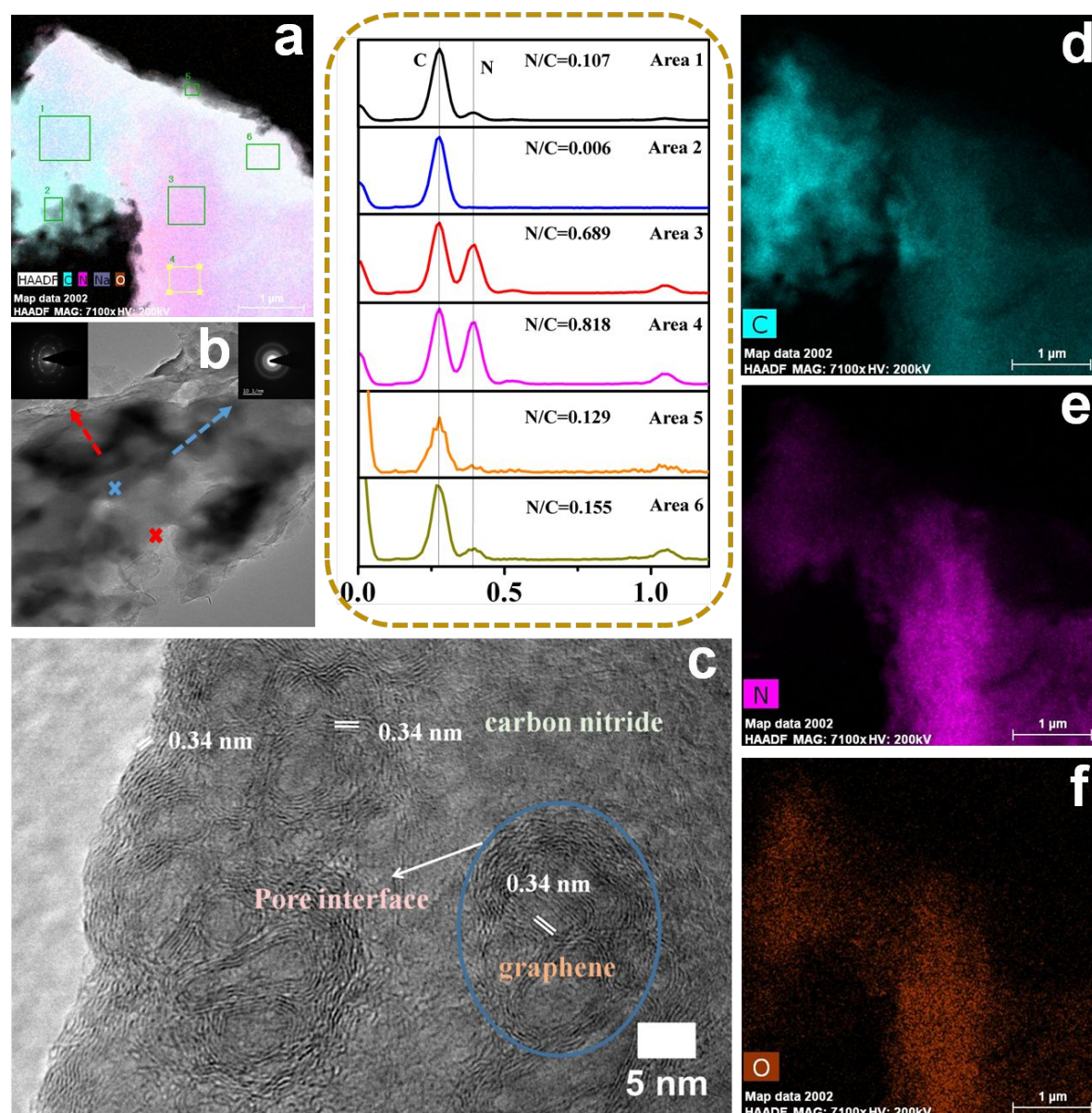


Figure 3. Macroscopic evidences of the formation of graphene/carbon nitride intralayer heterojunction. (a) High angle annular dark field scanning TEM images (HAADF-STEM) and corresponding EDX spectra of six areas of hydrogenated carbon nitride, different C/N ratio in EDX spectra indicated the filling in macropores of porous carbon nitride was graphene. (b-c) HRTEM image of reconstructed carbon nitride and selected-area electron diffraction images of two different areas. (d-f) Energy-dispersive X-ray spectroscopy (EDX) elemental mapping images of hydrogenated carbon nitride.

1
2
3 lattice spacing is 3.40 \AA^{12} and obvious boundaries (blue cycle in Figure 3c) can be found
4
5 between carbon nitride and graphene, indicating that the carbon grows along the cyclic edge of
6
7 macropores on the porous carbon nitride. In addition, the selected-area electron diffraction
8
9 image (inset of Figure 3b) proves the presence of the in-planar order of carbon and amorphous
10
11 carbon nitride. These results further confirm that the uniform graphene/carbon nitride intralayer
12
13 heterojunction was obtained.
14
15

16
17 Graphitic carbon nitride (bulk nanostructure), 2%- C_3N_4 and 6%- C_3N_4 (with bulk structure
18
19 and cyano groups at edge) and urea derived carbon nitride (porous without cyano groups) were
20
21 selected as contrast samples but failed to obtain graphene (Figure S17). Therefore, nano-pores
22
23 (confined spaces) and cyano groups at edge (active site) together are of crucial factors for the
24
25 graphene deposition at relatively low temperatures. The reaction rates on a planar solid surface
26
27 in open space, and that on the solid walls within a nano-pores (Figure 4a) were compared. Based
28
29 on the collision theory shown in equation 1,²⁵ the reaction rate of graphene growth is directly
30
31 proportional to the collision frequency.
32
33

$$r(T) = Z_p \exp\left(\frac{-E_a}{RT}\right) \quad \text{Eq. 1}$$

34
35 where Z is the collision frequency, E_a represents activation energy, R and T are constant and
36
37 temperature, respectively. In our case the reaction is between a diluted gaseous phase and the
38
39 reaction sites containing reactant B embedded in a solid surface. Considering a diluted gaseous
40
41 reactant A moved within the vicinity (one mean free path distance to) of a solid surface where
42
43 reactant B sites were embedded within a solid planar wall in open space, with all A molecules
44
45 moving perpendicularly towards the surface. A collision between the A molecule and the wall
46
47 will be likely to happen when the molecule is within the range of a mean free path to the wall,
48
49 which will result in a reaction when a type B molecule is simultaneously within a sphere of
50
51 diameter $r_{cs} = r_1 + r_2$ along the trajectory of the A molecule, where the radius of molecule A
52
53 and B are respectively r_1 and r_2 and r_{cs} represents the radius of the collision cross section
54
55
56
57
58
59
60

(Figure 4a). Within the time interval Δt the distance travelled by the molecule A is $v_{mean}\Delta t$, while the total number of A molecules enclosed

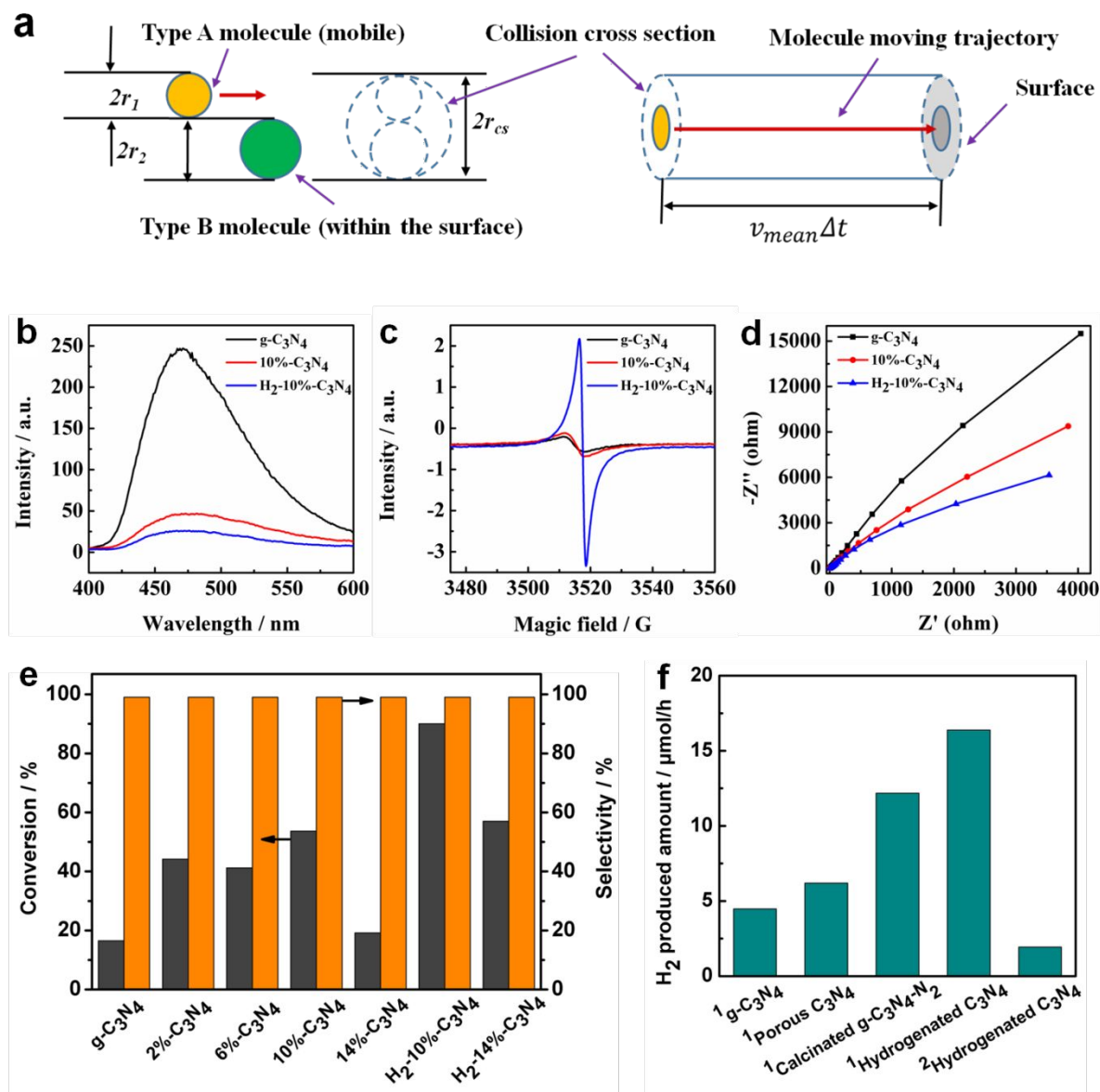


Figure 4. (a) A schematic graph of the collision process between a type A and a type B molecule, with collision cross section and path way distance demonstrated. (b) Fluorescence spectrum (PL). (c) Solid ESR spectra. (d) EIS spectra. (e) Selective photooxidation performances and (f) Photocatalytic performances on water splitting using the prepared samples. 1. Photocatalytic reaction conducted with > 420 nm filter and Pt as co-catalyst, and 2. without the filter and co-catalyst.

1
2
3 within the pathway of the cross section is $n_{+x} = Nv_{mean}\Delta t\pi r_{cs}^2/6$, where N is the number of
4
5 molecule A per volume, and v_{mean} represents the mean of the Maxwell-Boltzmann velocity
6
7 distribution of type A molecules. The reason for a denominator of 6 being included is that, the
8
9 molecules movement in a 3D space may be decomposed with respect to a Cartesian coordinate
10
11 system along 6 directions, *e.g.*, $\pm x$, $\pm y$, and $\pm z$, and that for a medium in equilibrium the
12
13 number of molecules moving along the $+x$ direction will be equal.
14
15
16

17 The collision frequency on a planar wall in open space can now be calculated as the ratio of
18
19 the total number of the type A molecules moving towards the wall over the length of the pass
20
21 way, *i.e.*,

$$Z_{wall} = \frac{n_{+x}}{v_{mean}\Delta t} = \frac{Nv_{mean}\Delta t\pi r_{cs}^2/6}{v_{mean}\Delta t} = \frac{N}{6}\pi r_{cs}^2 \quad \text{Eq. 2}$$

22
23
24
25
26
27 In contrast, with a nano-pore with a diameter, D , of the same order of magnitude with the mean
28
29 free path λ of the type A molecules, the situation is dramatically different even assuming other
30
31 conditions are unchanged. Here the geometrical constrain plays a key role, which affects the
32
33 molecules moving along 4 out of the 6 directions ($\pm x$ and $\pm y$). In this case a fraction of the
34
35 molecules currently moving in these 4 directions will strike into the wall of the nano-pore within
36
37 a single cycle along the path way before the next collision occurs. A comparative illustration
38
39 between a large pore (or a planar surface in open space) and a nano-pore is given in Figure S18a
40
41 and 18b. The quantitative expression of the collision frequency with a nano-pore can then be
42
43 given below,
44
45
46
47

$$Z_{pore} = \frac{n_{+x} + n_{-x} + n_{+y} + n_{-y}}{v_{mean}\Delta t} = \frac{4Nv_{mean}\Delta t\pi r_{cs}^2/6}{v_{mean}\Delta t} = \frac{2N}{3}\pi r_{cs}^2 \quad \text{Eq. 3}$$

48
49
50
51 Herein, a four-fold increase in the collision frequency, hence also in the reaction rate, would be
52
53 expected. In the case of this study, the typical nano-pore diameter is ~ 50 nm, which is compared
54
55 to the molecule mean free path in the air under standard pressure of 58 nm.²⁶ Then, a significant
56
57 increase in both collision frequency and the reaction rate inside the nano-pore, compared to that
58
59 on a planar surface in open space, is expected. Besides, it has been reported that the dissociation
60

energy for a H-N bond is 386 kJ/mol,²⁷ while the energy required for break one of the three bond is 355.3 kJ/mol,²⁸ with the latter being about 10 % lower than the former. Therefore, the cyano groups at the edge of nano-pores would also provide deposition sites for carbon free radical. Totally, combined the advantages from confined spaces and cyano groups, intralayered graphene/carbon nitride heterojunction *via* CEG process at low temperatures could be successfully obtained.

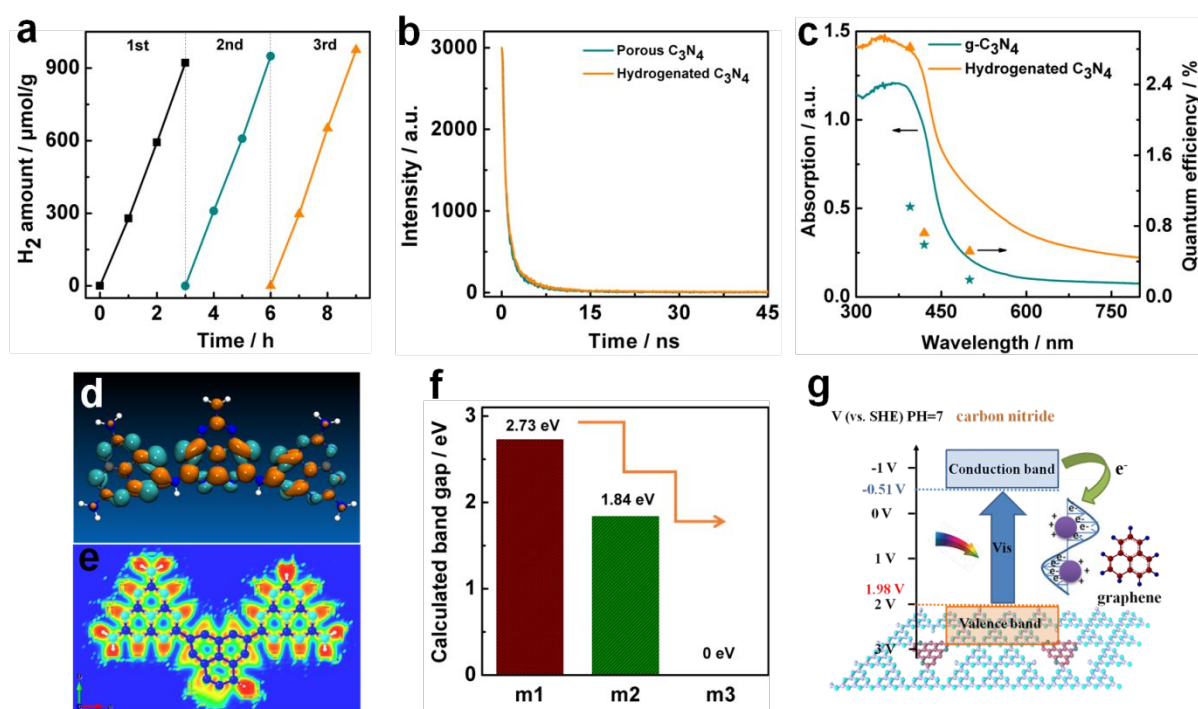


Figure 5. (a) Stability of hydrogenated carbon nitride in photocatalytic water splitting reaction with three cycles. (b) Time-resolved decay spectra of samples before and after the graphene deposition. (c) Wavelength dependent of quantum efficiency of g-C₃N₄ and hydrogenated C₃N₄. (d) DFT calculations of modules g-C₃N₄. (e) Electron localization function of hydrogenated carbon nitride, blue, white and cyan atoms represent carbon, hydrogen and nitrogen elements, respectively. (f) Calculated band gap of corresponding modellings of g-C₃N₄, porous carbon nitride as well as hydrogenated carbon nitride and (g) Diagram of electron transportation path in graphene/carbon nitride intralayered heterojunction.

1
2
3 After inserting nano-graphene into the lateral plane of carbon nitride, the light response
4 ability was improved. As shown in UV-Vis spectra (Figure S19a), g-C₃N₄ and 10%-C₃N₄ are
5 impeded by the weak light harvesting with almost no light response when the wavelength is
6 beyond 500 nm, while on H₂-10%-C₃N₄ obvious improvement could be observed in the full
7 visible region, even in NIR region this intralayered heterojunction still has response. This
8 enhancement is precisely attributed to the plasmonic effect of incorporated nano-graphene.²⁹
9
10 On this occasion, a photo-to-thermal experiment under inert atmosphere was conducted to
11 prove the effect of added plasmonic nano-graphene (Figure S19b). The temperature of g-C₃N₄
12 can increase to 97 °C within 30 min light irradiation mostly due to the heat dissipation from the
13 recombination of photoinduced charge carriers. While after adding trace amount (0.5 %) of
14 nano-graphene into the basal plane of carbon nitride (Table S2), the temperature is sharply
15 increased to 118 °C, which is comparable to that of graphene with same mass. Excluding the
16 heat generated from the the recombination of photo-induced electron-hole pairs on carbon
17 nitride, the extra elevated temperature on the hydrogenated carbon nitride (more than 20 °C)
18 confirms the enhanced electrical field on the graphene/carbon nitride heterojunction.^{30,31}
19 Moreover, the enhancement after the addition of graphene into the confined spaces of carbon
20 nitride was also verified using the finite element method. Embedding graphene nano-columns
21 into the confined spaces of porous carbon nitride has a dramatic impact over the original
22 homogenous electrical field (*E*) distribution (Figure S19 and Figure S20). High field
23 concentration is observed around the edge of the graphene nano-column. The electrical field is
24 plotted along a horizontal line, drawn around the top right corner of the graphene columns
25 where the local field maximum is found. A comparison is made between local intensity at the
26 maximum on the heterostructure and that on the plain g-C₃N₄ with the ratio $I/I_0 = (E/E_0)^2$ being
27 plotted in Figure S19c. The enhancement ripples the full spectrum and is wavelength dependent.
28 This observation is similar to the situation when metal nano-particals (NPs) are setting on
29 semiconductor substrate.³²
30
31
32
33
34
35
36
37
38
39
40
41
42
43
44
45
46
47
48
49
50
51
52
53
54
55
56
57
58
59
60

1
2
3 The separation rate of electron-hole pairs of carbon nitride is also boosted as a result of
4 surrounded electrical field from plasmonic nano-graphene. Indeed, the intensity of the PL peak
5 at 470 nm on porous carbon nitride reduced (Figure 4b and Figure S21) and the intensity of the
6 ESR characteristic peak of the unpaired electrons on the carbon nitride units rose (Figure 4c),
7 both indicating the recombination of photo-induced charge carriers was effectively prohibited
8 after the addition of nano-graphene.³³ Furthermore, the heterojunction exhibited a less
9 interfacial electron resistance due to the high electroconductibility of graphene (Figure 4d).

10
11
12 With suitable band structures (Figure S22-24 and Table S1) and enhanced electrical field,
13 the as-obtained carbon nitride sample was then evaluated for photoinduced selective oxidation
14 of 1,4-dihydro-2,6-dimethylpyridine-3,5-dicarboxylate (1,4-DHP) (Figure S25-27).^{22,34}
15 Pristine carbon nitride exerted a low conversion of 1,4-DHP (Figure 4e and Table S3) due to
16 the weak light response ability, and constraint of the Coulomb force for charge carriers. Once
17 the bulk carbon nitride was damaged to create the intralayer heterojunction at the edge plane of
18 macropores, the photooxidation rate of 1,4-DHP increased by almost three-fold on 10%-C₃N₄
19 with a conversion rate of 53.7 %. The conversion rate for photooxidation of 1,4-DHP
20 experienced a significant enhancement after introducing only 0.5 % plasmonic nano-graphene
21 onto carbon nitride intralayer, with 5.5 times improvement on H₂-10%-C₃N₄ compared to g-
22 C₃N₄. The prepared samples were also used for photocatalytic hydrogen evolution and 3.7 times
23 activity was acquired on hydrogenated carbon nitride than that of g-C₃N₄ (Figure 4f).
24 Meanwhile, hydrogenated carbon nitride showed a satisfied stability without any decrease on
25 photocatalytic hydrogen evolution ability after three cycle (Figure 5a). In particular, the metal-
26 free photocatalyst still exhibited photocatalytic ability on water splitting in the absence of co-
27 catalyst, with hydrogen evolution rate of 7720 $\mu\text{mol/h/g}_{\text{graphene}}$ under light irradiation
28 without >420 nm filter, which is higher than reported carbon/carbon nitride composites (Table
29 S4). As re-sintering of carbon nitride resulted in the interlayer stripping, the influence of heating
30 under N₂ rather than hydrogen atmosphere on the carbon nitride was also studied. The
31
32
33
34
35
36
37
38
39
40
41
42
43
44
45
46
47
48
49
50
51
52
53
54
55
56
57
58
59
60

1
2
3 photocatalytic hydrogen evolution rate of calcinated g-C₃N₄-N₂ was 12.2 μmol/h, which was
4
5 lower than that of hydrogenated carbon nitride (16.4 μmol/h) (Figure 4f), suggesting that the
6
7 self-assembly of nano-graphene into carbon nitride is more efficient for the catalyst
8
9 modification. Furthermore, the time-resolved decay spectra of samples before and after the
10
11 graphene deposition were obtained for confirming the enhanced performance. As shown in
12
13 Figure 5b and Table S5, the average lifetime of hydrogenated carbon nitride was 2.14 ns, which
14
15 was longer than the sample before the graphene deposition (1.99 ns). Meanwhile, a higher
16
17 visible light irradiated photocurrent was obtained in H₂-10%-C₃N₄ than g-C₃N₄ and 10%-C₃N₄,
18
19 further demonstrating the higher efficiency in the separation of photo-induced charge carriers
20
21 on the advanced metal-free photocatalyst (Figure S28). As a result, the quantum efficiency of
22
23 hydrogenated carbon nitride at 395, 420 and 500 nm were all higher than that of g-C₃N₄ (Figure
24
25 5c).

26
27
28
29
30
31 The improvement on light absorption and photocatalytic performances after the graphene
32
33 formation was proven by DFT calculations (Figure 5d-f), in which part of m1 (Figure 5d), m2
34
35 (Figure S29b) and m3 (Figure 5e) molecules are employed as they represent the characteristics
36
37 of the corresponding samples and are able to affect the optical and electrochemical properties
38
39 of the relevant intact structures. The porous carbon nitride and hydrogenated carbon nitride
40
41 presented lowered band gap energies by comparison to g-C₃N₄. In particular, the m3 structure
42
43 exhibited partial metallicity with band gap 0 eV, demonstrating the enhanced optical property
44
45 of H₂-10%-C₃N₄. To unveil the effect of the fabricated heterostructure on the electronic
46
47 structure of carbon nitride, frontier molecular orbitals were examined (Figure 5 and Figure S29).
48
49 With the g-C₃N₄ system, the LUMO is mainly consisted of C–N bonding orbitals and HOMO
50
51 is derived from the heterocyclic nitrogen P_z orbitals.³⁴ On the porous carbon nitride system, the
52
53 LUMO shifts from the melem to the damaged unit, while the HOMO mainly locates on the
54
55 melem moiety, indicative of promoted separation of charge carriers. After incorporation of the
56
57 carbon ring into hydrogenated carbon nitride, the electrons between some of the C=C bonding
58
59
60

1
2
3 of carbon rings were not well localized and exhibited partial metallization. As the partial
4 metallization of the joint on intralayer heterojunction enabled more free electrons assembled,
5 enhanced electrical field could be obtained on this area. These results are consistent with that
6 calculated by FE method. As a result, combined DFT and FE calculations, conclusions could
7 be reached that on one side, the heterostructure of obtained photocatalyst enhances the electrical
8 field which compels the charge carriers out of the constraint of the Coulomb force. On the
9 other hand, the formed graphene acts as the transferring channel of photoinduced electron, both
10 effectively prohibiting the recombination of electron/hole pairs for redox reactions. (Figure 5g).
11
12
13
14
15
16
17
18
19
20
21

22 CONCLUSIONS

23
24
25
26 In summary, we proposed a hydrogen-initiated chemical epitaxial growth strategy to fabricate
27 intralayered polymer based heterojunction. Compared with the traditional CVD method, this
28 strategy can be realized at relatively low temperatures as a result of the confined space and
29 active site. Combined the experimental and computational methods, the acquired in-plane
30 heterojunction exhibits enhanced electrical field and a more efficient electronic structure to
31 facilitate carriers' separation and transfer. As a result, this photocatalyst was shown to possess
32 better performances on artificial synthesis. This work is expected to shed light in further
33 improvement of CEG process for constructing metal-free photocatalysts in order to achieve
34 feasible photosynthesis.
35
36
37
38
39
40
41
42
43
44
45
46
47

48 METHODS

49
50
51 **Damage of bulk structured carbon nitride.** Porous carbon nitride was prepared by a soft
52 template method. Typically, 5 g melamine and sodium bicarbonate (the mass varied from 0.1,
53 0.3, 0.5 to 0.7 g to respectively synthesize 2%-C₃N₄, 6%-C₃N₄, 10%-C₃N₄ and 14%-C₃N₄) were
54 both dissolved in ultrapure water and subsequently heated at 100 °C for water evaporation.
55 After that, the obtained precursor was fully ground with an agate mortar and put into a furnace.
56
57
58
59
60

1
2
3 Heat treatment of the precursor was done at 823 K for 4 h with a heating rate of 2.3 K min⁻¹.
4
5 After the calcination, the samples were thoroughly washed by hot water and ethanol for several
6
7 times and subsequently dried at 333 K overnight to obtain the porous carbon nitride. For
8
9 comparison, a sample of bulk g-C₃N₄ was synthesized by the same synthesis procedure without
10
11 using the soft template of sodium bicarbonate.
12
13
14

15 **Modified chemical epitaxial growth strategy for graphene/carbon nitride intralayered**
16 **heterojunctions.** Initially, a certain amount of the prepared porous carbon nitride was put into
17
18 a quartz U-tube which was then put into a temperature programmed heating jacket. The U tube
19
20 was degassed at 523 K with N₂ for 2 h. Then the gas was changed to H₂/N₂ mixture with the
21
22 concentration of H₂ 5% and the degassed sample was heated to 773 K at a heating rate of 5
23
24 K/min. After the temperature arrived at 773 K, it was naturally cooled to room temperature to
25
26 obtain the hydrogenated carbon nitride. The influence of heating under inert gas rather than
27
28 hydrogen atmosphere on the carbon nitride was also studied with the same reaction condition
29
30 but the hydrogen atmosphere was replaced by the ultra-pure nitrogen. The obtained sample was
31
32 named as calcinated g-C₃N₄-N₂.
33
34
35
36
37
38
39

40 **Characterizations.** The structures of the prepared photocatalysts were characterized through
41
42 the X-ray diffraction (X'Pert PRO MPD, Holland). N₂ adsorption-desorption isotherms were
43
44 obtained from a Micromeritics Tristar 3000 at 77 K. Scanning electron microscope images were
45
46 captured on a FEI Verios XHR 460. Transmission electron microscope and HRTEM images
47
48 were recorded on a JEOL 2100. HAADF-STEM and EDX elemental mapping were performed
49
50 by a FEI Titan G2 80-200 TEM/STEM. XPS measurements were performed using a Kratos
51
52 Axis Ultra DLD spectrometer with an Al K α (1486 eV) X-ray source operating at 225W.
53
54 NEXAFS tests were carried out with the Soft X-Ray beamline from the Australian
55
56 Synchrotron³⁵ and conducted at room temperature under the conditions of ultra-high vacuum
57
58 (UHV). All spectra were collected in the partial electron yield (PEY) mode using an electron
59
60

1
2
3 flood gun to adequately neutralise the sample. The normalizing of all the NEXAFS spectra was
4 processed with the QANT software program developed by the Australian Synchrotron.³⁶ AFM
5 images were collected by a Bruker icon equipment. Solid-state ¹³C Direct Polarization (DP)
6 and Cross-Polarisation (CP) MAS NMR spectra were obtained on a Varian VNMRS WB
7 spectrometer (¹H 399.868 MHz, ¹³C 100.554 MHz) equipped with a 4 mm MAS probe. XPS
8 measurements were performed using a Kratos Axis Ultra DLD spectrometer with an Al K α
9 (1486 eV) X-ray source operating at 225W. Survey spectra were obtained employing a pass
10 energy of 160 eV, whilst all high resolution spectra was collected *via* a pass energy of 40 eV.
11 The binding energy scale of all XPS spectra were calibrated by locking the C1s peak to 284.5
12 eV. Solid-state ¹³C Direct Polarization (DP) and Cross-Polarisation (CP) MAS NMR spectra
13 were obtained on a Varian VNMRS WB spectrometer (¹H 399.868 MHz, ¹³C 100.554 MHz)
14 equipped with a 4 mm MAS probe. All samples were spun at 7 kHz in 4 mm zircon rotors with
15 kel-F caps. A 90° pulse of 5 us, contact time of 2 ms (CP-MAS) and recycle times of 2 and 60
16 seconds were used for the CP-MAS and DP-MAS experiments, respectively. For all
17 experiments, 1K data points were collected, and zero-filled to 8K points, with a line broadening
18 of 100 Hz applied. Chemical shifts were determined against an external adamantane standard
19 (38.5 ppm) and are reported relative to tetramethylsilane (0 ppm). Fourier transform infrared
20 (FT-IR) spectra were collected on a PerkinElmer instrument. Diffused reflectance spectra and
21 photoluminescence spectra (PL) were recorded on a Cary 100 UV-vis Spectrophotometer and
22 a Cary Eclipse Fluorescence Spectrophotometer (Agilent, US), respectively. The time-resolved
23 decay spectra was performed on a FLS1000 with the excitation and detection wavelengths were
24 375 and 460 nm, respectively.

25
26
27
28
29
30
31
32
33
34
35
36
37
38
39
40
41
42
43
44
45
46
47
48
49
50
51
52
53
54
55 ***In situ* detection of effluent gases under H₂ or N₂ calcination.** Porous carbon nitride was
56 placed in a sealed tube furnace, which was connected with an online gas chromatograph (GC,
57 Agilent 7820A). H₂ or N₂ was purged into the reactor for fully replacing the air inside. Then
58
59
60

1
2
3 the furnace was heated and the effluent gases were analyzed by gas chromatograph equipped
4 with Porapak N and Molsieve 5A columns.
5
6
7

8 **Photoinduced selective oxidation of 1,4-DHP.** The photooxidation tests were conducted in
9 a customized reactor. The aqueous solution (50 mL) dispersing 10^{-4} mol/L of 1,4-DHP and
10 samples (30.0 mg) was irradiated by a LED solar simulator (Newport). After 1 h, the conversion
11 of 1,4-DHP was monitored by a Cary 100 UV-vis Spectrophotometer.
12
13
14
15
16
17

18 **Photocatalytic water splitting.** The H_2 evolution tests were performed by using a LabSolar-
19 III AG reaction system (Beijing PerfectLight Co.). Photocatalyst (50 mg) was dispersed into a
20 50 mL of aqueous solution containing 5 mL of TEOA, and 0.8 mL $H_2PtCl_6 \cdot (H_2O)_6$ (3.0 wt%).
21 Before the irradiation, the reaction cell was sealed to thoroughly evacuate for 40 min to remove
22 air. A Xe lamp (300 W) (CEL-HXF300, Beijing Cel Sci-tech Co., Ltd.) equipped with a 420
23 nm cut-off filter was employed as the visible light source. The reaction system was kept at 6 °C
24 using the cooling water. The generated hydrogen was detected with an online gas
25 chromatograph (GC7920) equipped with a 5A molecular sieve column and a thermal
26 conductive detector (TCD). N_2 was employed as the carrier gas. Same reaction without
27 $H_2PtCl_6 \cdot (H_2O)_6$ as co-catalyst and without cut-off filter was also performed. Besides, the
28 stability of hydrogenated carbon nitride was studied in water splitting reaction with three cycles.
29 In addition, the quantum efficiency of photocatalytic water splitting reaction was tested under
30 the irradiations of monochromatic light including 395, 420 and 500 nm.
31
32
33
34
35
36
37
38
39
40
41
42
43
44
45
46
47
48
49

50 **Photo-to-thermal tests.** 50 mg sample was dispersed uniformly on a quartz microfiber filter
51 which was sealed in a quartz reactor. A thermocouple was contacted with the surface of filter
52 for monitoring the temperature of sample. Before reaction, the reactor was replaced by Ar for
53 2 h to make sure no air inside. Then light with 1 W/cm^2 was irradiated on the sample and
54 simultaneously the temperature of sample was recorded at certain time intervals.
55
56
57
58
59
60

1
2
3 **Simulation details.** Vienna Ab initio Simulations Package (VASP) was used to perform the
4 DFT simulations.^{37,38} The projected augmented wave (PAW) method and generalized gradient
5 approximation (GGA) in the Perdew, Burke and Ernzerhof (PBE)³⁹ parameterization were used.
6
7 The molecule fragments were modelled in a $35 \times 18 \times 15 \text{ \AA}^3$ supercell, which allows at least a
8 distance of 10 \AA between images in any dimension. The first Brillouin zone was sampled by
9 using a Gamma-centred \mathbf{k} -point set of $1 \times 2 \times 2$. The plane-wave cutoff energy was set to be 400
10 eV. The coordinates were fully relaxed, and the energy and force were converged within 10^{-4}
11 eV/cell and 10^{-2} eV/\AA , respectively.
12
13

14
15
16
17
18
19
20
21
22
23 The finite element modelling (FEM) is on the basis of classical electro-magnetic field theory
24 employed to obtain the electrical field by solving Maxwell equations. COMSOL Multiphysics
25 software⁴⁰ was used for modelling the plasmonic effect within the carbon nitride/graphene
26 structure. The size of the simulation domain was of the same order of magnitude with the optical
27 wavelength, so that the effect of the wavelength variation can be accurately evaluated. A FEM
28 model is constructed with the upper part of the domain filled with water while the lower part is
29 filled with the g-C₃N₄ materials, separated by a p horizontal boundary. A graphene column with
30 a diameter of 50 nm is embedded at the centre of g-C₃N₄ material. For comparison purpose the
31 second model of plain g-C₃N₄ block was built. Perfect matching layers (PMLs) were defined
32 both at the top and at the bottom of the model, which were designed to completely absorb all
33 the reflected and transmitted waves with arbitrary wave front, respectively, so as to remove any
34 interference of back-reflected waves from the top and bottom. For all of the FEM modelling
35 results presented in this work, an incident radiation is set at the top, transmitting downwards
36 with an intensity of 10^4 W/m^2 .
37
38
39
40
41
42
43
44
45
46
47
48
49
50
51
52
53
54

55 ASSOCIATED CONTENT

56 Supporting Information

1
2
3 The supporting Information is available free of charge on the ACS Publications website at DOI:
4
5 Details of experimental section, textural properties, chemical compositions, TEM, SEM
6
7 and AFM images, FT-IR, nitrogen isotherms, XPS-VB, photooxidation performances of
8
9 1,4-DHP, photocurrent curves, FEM and DFT simulations; additional supplementary
10
11 figures, tables, and text referenced in the article. (PDF)
12
13
14

15 16 **AUTHOR INFORMATION**

17 18 **Corresponding Authors**

19
20
21 **Hongqi Sun** – School of Engineering, Edith Cowan University, 270 Joondalup Drive,
22
23 Joondalup, WA 6027, Australia; orcid.org/0000-0003-0907-5626; Email: h.sun@ecu.edu.au

24
25
26 **Shaobin Wang** – School of Chemical Engineering and Advanced Materials, The University of
27
28 Adelaide, Adelaide, SA 5005, Australia; Email: shaobin.wang@adelaide.edu.au

29 30 **Authors**

31
32
33 **Jinqiang Zhang** – School of Engineering, Edith Cowan University, 270 Joondalup Drive,
34
35 Joondalup, WA 6027, Australia

36
37
38 **Yunguo Li** – Department of Earth Sciences, University College London, Gower Street, London
39
40 WC1E 6BT, UK

41
42
43 **Xiaoli Zhao** – School of Engineering, Edith Cowan University, 270 Joondalup Drive,
44
45 Joondalup, WA 6027, Australia

46
47
48 **Huayang Zhang** – School of Chemical Engineering and Advanced Materials, The University
49
50 of Adelaide, Adelaide, SA 5005, Australia

51
52
53 **Liang Wang** – State Key Laboratory of Mater-Oriental Chemical Engineering, College of
54
55 Chemistry and Chemical Engineering, Nanjing Tech University, Nanjing 210009, China

56
57
58 **Haijun Chen** – Jiangsu Key Laboratory of Process Enhancement and New Energy Equipment
59
60 Technology, Jiangsu Engineering Laboratory of Energy Conservation and Environmental

1
2
3 Protection Technologies and Equipment in Process Industry, School of Mechanical and Power
4 Engineering, Nanjing Tech University, Nanjing 211816, China

5
6
7 **Shuaijun Wang** – School of Engineering, Edith Cowan University, 270 Joondalup Drive,
8 Joondalup, WA 6027, Australia

9
10
11 **Xinyuan Xu** – School of Engineering, Edith Cowan University, 270 Joondalup Drive,
12 Joondalup, WA 6027, Australia

13
14
15 **Lei Shi** – School of Engineering, Edith Cowan University, 270 Joondalup Drive, Joondalup,
16 WA 6027, Australia

17
18
19 **Lai-Chang Zhang** – School of Engineering, Edith Cowan University, 270 Joondalup Drive,
20 Joondalup, WA 6027, Australia

21
22
23 **Jean-Pierre Veder** – John de Laeter Centre, Curtin University, Perth, Western Australia 6102,
24 Australia

25
26
27 **Shiyong Zhao** – Fuels and Energy Technology Institute & Western Australia School of Mines:
28 Minerals, Energy and Chemical Engineering, Curtin University, Perth, Western Australia 6102,
29 Australia

30
31
32 **Gareth Nealon** – Centre for Microscopy, Characterisation and Analysis, The University of
33 Western Australia, Crawley, WA 6009, Australia

34
35
36 **Mingbo Wu** – State Key Laboratory of Heavy Oil Processing, Institute of New Energy, College
37 of Chemical Engineering, China University of Petroleum (East China), Qingdao, 266580, China

38
39
40 **Shaobin Wang** – School of Chemical Engineering and Advanced Materials, The University of
41 Adelaide, Adelaide, SA 5005, Australia; orcid.org/0000-0002-1751-9162

42
43
44 **Hongqi Sun** – School of Engineering, Edith Cowan University, 270 Joondalup Drive,
45 Joondalup, WA 6027, Australia; orcid.org/0000-0003-0907-5626

46
47
48 **Author Contributions**

1
2
3 The manuscript was written through contributions of all authors. All authors have given
4 approval to the final version of the manuscript.
5
6

7 **Notes**

8
9 The authors declare no competing financial interest.
10
11
12

13 **ACKNOWLEDGEMENTS**

14
15
16 The author (Sun) would like to express his thanks for the support from ECU Vice-Chancellor's
17 Professorial Research Fellowship. This work was partially supported by the Australian
18 Research Council (DP170104264 and DP190103548). The authors acknowledge the assistance
19 from the Centre for Microscopy, Characterisation and Analysis of the University of Western
20 Australia, and the WA X-Ray Surface Analysis Facility of Curtin University, funded by an
21 Australian Research Council LIEF grant (LE120100026). The authors also thank the valuable
22 advices and technical supports provided by B. Cowie and L. Thompsen regarding NEXAFS
23 tests. All NEXAFS measurements were conducted on the soft X-ray beamline of the Australian
24 Synchrotron, Victoria, Australia, part of ANSTO.
25
26
27
28
29
30
31
32
33
34
35
36
37

38 **REFERENCES**

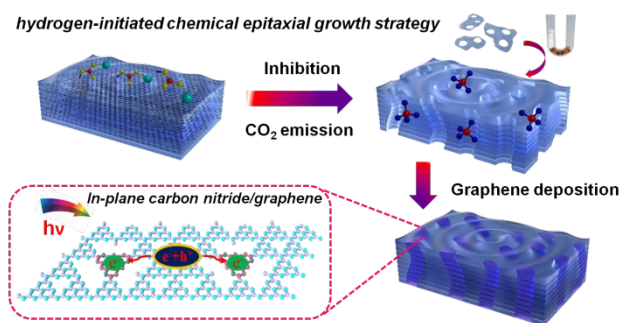
- 39
40
41
42 1. Shoji, S.; Peng, X.; Yamaguchi, A.; Watanabe, R.; Fukuhara, C.; Cho, Y.; Yamamoto,
43 T.; Matsumura, S.; Yu, M.-W.; Ishii, S.; Fujita, T.; Abe, H.; Miyauchi, M., Photocatalytic
44 Uphill Conversion of Natural Gas beyond the Limitation of Thermal Reaction Systems. *Nat.*
45 *Catal.* **2020**, *3*, 148-153.
46
47 2. Fu, M.; Shang, R.; Zhao, B.; Wang, B.; Fu, Y., Photocatalytic Decarboxylative
48 Alkylations Mediated by Triphenylphosphine and Sodium Iodide. *Science* **2019**, *363*, 1429-
49 1434.
50
51 3. Sun, H.; Zhou, G.; Wang, Y.; Suvorova, A.; Wang, S., A New Metal-Free Carbon
52 Hybrid for Enhanced Photocatalysis. *ACS Appl. Mater. Interfaces* **2014**, *6*, 16745-16754.
53
54 4. Zheng, Y.; Jiao, Y.; Zhu, Y.; Li, L. H.; Han, Y.; Chen, Y.; Du, A.; Jaroniec, M.; Qiao,
55 S. Z., Hydrogen Evolution by a Metal-Free Electrocatalyst. *Nat. Commun.* **2014**, *5*, 3783-3791.
56
57
58
59
60

- 1
2
3 5. Yu, Q.; Jauregui, L. A.; Wu, W.; Colby, R.; Tian, J.; Su, Z.; Cao, H.; Liu, Z.; Pandey,
4 D.; Wei, D.; Chung, T. F.; Peng, P.; Guisinger, N. P.; Stach, E. A.; Bao, J.; Pei, S.-S.; Chen, Y.
5 P., Control and Characterization of Individual Grains and Grain Boundaries in Graphene Grown
6 by Chemical Vapour Deposition. *Nat. Mater.* **2011**, *10*, 443-449.
- 7
8
9 6. Kim, H.; Miura, Y.; Macosko, C. W., Graphene/Polyurethane Nanocomposites for
10 Improved Gas Barrier and Electrical Conductivity. *Chem. Mater.* **2010**, *22*, 3441-3450.
- 11
12 7. Zhou, P.; Yu, J.; Jaroniec, M., All-Solid-State Z-Scheme Photocatalytic Systems. *Adv.*
13 *Mater.* **2014**, *26*, 4920-4935.
- 14
15
16 8. Liu, L.; Park, J.; Siegel, D. A.; McCarty, K. F.; Clark, K. W.; Deng, W.; Basile, L.;
17 Idrobo, J. C.; Li, A. P.; Gu, G., Heteroepitaxial Growth of Two-Dimensional Hexagonal Boron
18 Nitride Templated by Graphene Edges. *Science* **2014**, *343*, 163-167.
- 19
20
21 9. Liu, Z.; Ma, L.; Shi, G.; Zhou, W.; Gong, Y.; Lei, S.; Yang, X.; Zhang, J.; Yu, J.;
22 Hackenberg, K. P.; Babakhani, A.; Idrobo, J. C.; Vajtai, R.; Lou, J.; Ajayan, P. M., In-Plane
23 Heterostructures of Graphene and Hexagonal Boron Nitride with Controlled Domain Sizes. *Nat.*
24 *Nanotechnol.* **2013**, *8*, 119-124.
- 25
26
27 10. Liu, Y.; Huang, Y.; Duan, X., Van der Waals Integration before and beyond Two-
28 Dimensional Materials. *Nature* **2019**, *567*, 323-333.
- 29
30
31 11. Che, W.; Cheng, W.; Yao, T.; Tang, F.; Liu, W.; Su, H.; Huang, Y.; Liu, Q.; Liu, J.; Hu,
32 F.; Pan, Z.; Sun, Z.; Wei, S., Fast Photoelectron Transfer in (Cring)-C₃N₄ Plane Heterostructural
33 Nanosheets for Overall Water Splitting. *J. Am. Chem. Soc.* **2017**, *139*, 3021-3026.
- 34
35
36 12. Huang, C.; Chen, C.; Zhang, M.; Lin, L.; Ye, X.; Lin, S.; Antonietti, M.; Wang, X.,
37 Carbon-Doped BN Nanosheets for Metal-Free Photoredox Catalysis. *Nat. Commun.* **2015**, *6*,
38 7698-7705.
- 39
40
41 13. Cai, Z.; Liu, B.; Zou, X.; Cheng, H. M., Chemical Vapor Deposition Growth and
42 Applications of Two-Dimensional Materials and Their Heterostructures. *Chem. Rev.* **2018**, *118*,
43 6091-6133.
- 44
45
46 14. Li, H.; Li, Y.; Aljarb, A.; Shi, Y.; Li, L.-J., Epitaxial Growth of Two-Dimensional
47 Layered Transition-Metal Dichalcogenides: Growth Mechanism, Controllability, and
48 Scalability. *Chem. Rev.* **2017**, *118*, 6134-6150.
- 49
50
51 15. Tian, W.; Zhang, H.; Sun, H.; Suvorova, A.; Saunders, M.; Tade, M.; Wang, S.,
52 Heteroatom (N or N-S)-Doping Induced Layered and Honeycomb Microstructures of Porous
53 Carbons for CO₂ Capture and Energy Applications. *Adv. Funct. Mater.* **2016**, *26*, 8651-8661.
- 54
55
56
57
58
59
60

- 1
2
3 16. Tang, H.; Xiong, F.; Jiang, Y.; Pei, C.; Tan, S.; Yang, W.; Li, M.; An, Q.; Mai, L., Alkali
4 Ions Pre-Intercalated Layered Vanadium Oxide Nanowires for Stable Magnesium Ions Storage.
5 *Nano Energy* **2019**, *58*, 347-354.
6
7
8 17. Tay, Q.; Kanhere, P.; Ng, C. F.; Chen, S.; Chakraborty, S.; Huan, A. C. H.; Sum, T. C.;
9 Ahuja, R.; Chen, Z., Defect Engineered g-C₃N₄ for Efficient Visible Light Photocatalytic
10 Hydrogen Production. *Chem. Mater.* **2015**, *27*, 4930-4933.
11
12
13 18. Yu, H.; Shi, R.; Zhao, Y.; Bian, T.; Zhao, Y.; Zhou, C.; Waterhouse, G. I. N.; Wu, L.
14 Z.; Tung, C. H.; Zhang, T., Alkali-Assisted Synthesis of Nitrogen Deficient Graphitic Carbon
15 Nitride with Tunable Band Structures for Efficient Visible-Light-Driven Hydrogen Evolution.
16 *Adv. Mater.* **2017**, *29*, 1605148-1605155.
17
18
19 19. Hosmane, R. S.; Rossman, M. A.; Leonard, N. J., Synthesis and Structure of Tri-s-
20 triazine. *J. Am. Chem. Soc.* **1982**, *104*, 5497-5499.
21
22
23 20. Gao, W.; Alemany, L. B.; Ci, L.; Ajayan, P. M., New Insights into the Structure and
24 Reduction of Graphite Oxide. *Nat. Chem.* **2009**, *1*, 403-408.
25
26
27 21. Akaike, K.; Aoyama, K.; Dekubo, S.; Onishi, A.; Kanai, K., Characterizing Electronic
28 Structure near the Energy Gap of Graphitic Carbon Nitride Based on Rational Interpretation of
29 Chemical Analysis. *Chem. Mater.* **2018**, *30*, 2341-2352.
30
31
32 22. Wu, W.; Zhang, J.; Fan, W.; Li, Z.; Wang, L.; Li, X.; Wang, Y.; Wang, R.; Zheng, J.;
33 Wu, M.; Zeng, H., Remedying Defects in Carbon Nitride to Improve Both Photooxidation and
34 H₂ Generation Efficiencies. *ACS Catal.* **2016**, *6*, 3365-3371.
35
36
37 23. Duan, X.; O'Donnell, K.; Sun, H.; Wang, Y.; Wang, S., Sulfur and Nitrogen Co-Doped
38 Graphene for Metal-Free Catalytic Oxidation Reactions. *Small* **2015**, *11*, 3036-3044.
39
40
41 24. Guo, F.; Yang, P.; Pan, Z.; Cao, X.-N.; Xie, Z.; Wang, X., Carbon-Doped BN
42 Nanosheets for the Oxidative Dehydrogenation of Ethylbenzene. *Angew. Chem., Int. Ed.* **2017**,
43 *56*, 8231-8235.
44
45
46 25. McNaught, A. D.; McNaught, A. D., *Compendium of chemical terminology*. Blackwell
47 Science Oxford: 1997; Vol. 1669.
48
49
50 26. Jennings, S., The Mean Free Path in Air. *J. Aerosol Sci.* **1988**, *19*, 159-166.
51
52
53 27. Benson, S. W., III-Bond Energies. *J. Chem. Edu.* **1965**, *42*, 502-518.
54
55 28. Alkorta, I.; Elguero, J., Dissociation Energies and Rotational Barriers about CC Single,
56 Double, and Triple Bonds: A Hybrid HF-DFT Approach (Becke3LYP/6-311++ G**). *Struct.*
57 *Chem.* **1998**, *9*, 59-63.
58
59
60

- 1
2
3 29. Meng, X.; Wang, T.; Liu, L.; Ouyang, S.; Li, P.; Hu, H.; Kako, T.; Iwai, H.; Tanaka, A.;
4 Ye, J., Photothermal Conversion of CO₂ into CH₄ with H₂ over Group VIII Nanocatalysts: An
5 Alternative Approach for Solar Fuel Production. *Angew. Chem. Int. Ed.* **2014**, *53*, 11478-11482.
6
7 30. Govorov, A. O.; Zhang, H.; Demir, H. V.; Gun'ko, Y. K., Photogeneration of Hot
8 Plasmonic Electrons with Metal Nanocrystals: Quantum Description and Potential Applications.
9 *Nano Today* **2014**, *9*, 85-101.
10
11 31. Aslam, U.; Chavez, S.; Linic, S., Controlling Energy Flow in Multimetallic
12 Nanostructures for Plasmonic Catalysis. *Nat. Nanotechnol.* **2017**, *12*, 1000-1005.
13
14 32. Liu, X.; Swihart, M. T. J. C. S. R., Heavily-Doped Colloidal Semiconductor and Metal
15 Oxide Nanocrystals: An Emerging New Class of Plasmonic Nanomaterials. *Chem. Soc. Rev.*
16 **2014**, *43*, 3908-3920.
17
18 33. Zhang, J.; Zhang, G.; Chen, X.; Lin, S.; Mohlmann, L.; Dolega, G.; Lipner, G.;
19 Antonietti, M.; Blechert, S.; Wang, X., Co-Monomer Control of Carbon Nitride
20 Semiconductors to Optimize Hydrogen Evolution with Visible Light. *Angew. Chem. Int. Ed.*
21 **2012**, *51*, 3183-3187.
22
23 34. Zhang, J.; An, X.; Lin, N.; Wu, W.; Wang, L.; Li, Z.; Wang, R.; Wang, Y.; Liu, J.; Wu,
24 M., Engineering Monomer Structure of Carbon Nitride for the Effective and Mild
25 Photooxidation Reaction. *Carbon* **2016**, *100*, 450-455.
26
27 35. Watts, B.; Swaraj, S.; Nordlund, D.; Luning, J.; Ade, H., Calibrated NEXAFS Spectra
28 of Common Conjugated Polymers. *J. Chem. Phys.* **2011**, *134* (2), 024702-024717.
29
30 36. Gann, E.; McNeill, C. R.; Tadich, A.; Cowie, B. C.; Thomsen, L., Quick AS NEXAFS
31 Tool (QANT): A Program for NEXAFS Loading and Analysis Developed at the Australian
32 Synchrotron. *J. Synchrotron Radiat.* **2016**, *23* (1), 374-380.
33
34 37. Kresse, G.; Joubert, D., From Ultrasoft Pseudopotentials to the Projector Augmented-
35 Wave Method. *Phys. Rev. B* **1999**, *59* (3), 1758-1775.
36
37 38. Blöchl, P. E., Projector Augmented-Wave Method. *Phys. Rev. B* **1994**, *50* (24), 17953-
38 17979.
39
40 39. Perdew, J. P.; Burke, K.; Ernzerhof, M., Generalized Gradient Approximation Made
41 Simple. *Phys. Rev. Lett.* **1996**, *77* (18), 3865-3868.
42
43 40. Pryor, R. W., *Multiphysics Modeling Using COMSOL: A First Principles Approach*;
44 Jones & Bartlett Publishers: Burlington, 2009.
45
46
47
48
49
50
51
52
53
54
55
56
57
58
59
60

Table of Contents Entry



We *in situ* deposited nano-graphene along confined spaces with active site of porous carbon nitride. The performances in both selective photooxidation and photocatalytic water splitting were improved owing to the enhanced electrical field and a more efficient electronic structure from the addition of trace amount of plasmonic nano-graphene.